J Nanopart Res (2010) 12:2081–2092
DOI 10.1007/s11051-009-9767-y

RESEARCH PAPER

The effects of vacuum annealing on the structure and surface chemistry of iron:nickel alloy nanoparticles

Michelle Dickinson · Thomas B. Scott · Richard A. Crane · Olga Riba · Robert J. Barnes · Gareth M. Hughes

Received: 9 April 2009 / Accepted: 21 September 2009 / Published online: 16 October 2009

Abstract In order to increase the longevity of contaminant retention on the particle surface, a method is sought to improve the corrosion resistance of bimetallic iron nickel nanoparticles (INNP) used for the remediation of contaminated water, and thereby extend their industrial lifetime. A multi-disciplinary approach was used to investigate changes induced by vacuum annealing ($<5 \times 10^{-8}$ mbar) at 500 °C on the bulk and surface chemistry of INNP. The particle size was determined to increase significantly as a result of annealing and the thickness of the surface oxide increased by 50%. BET analysis recorded a decrease in INP surface area from 44.88 to 8.08 $m^2\ g^{-1}$, consistent with observations from scanning electron microscopy (SEM) and transmission electron microscopy (TEM) which indicated the diffusion bonding of previously discrete particles at points of contact. X-ray diffraction (XRD) confirmed that recrystallisation of the metallic cores had occurred, converting a significant fraction of initially amorphous iron nickel alloy into crystalline FeNi alloy. X-ray photoelectron spectroscopy (XPS) indicated a reduction in the proportion of surface iron oxide and a change in its stoichiometry related to annealing-induced disproportionation. This was also evidenced by an increased proportion of Fe(0) and Ni(0) to Fe- and Ni-oxides, respectively. The data also indicated the concurrent development of boron oxide at the metal surfaces, which accounts for the overall increase measured in surface oxide thickness. The improved core crystallinity and the presence of passivating impurity phases at the INNP surfaces may act to improve the corrosion resistance and reactive lifespan of the vacuum annealed INNP for environmental applications.

Keywords Iron · Nickel · Nanoparticles · Anneal · XPS · Remediation of contaminated waters · EHS

M. Dickinson (✉) · T. B. Scott · R. A. Crane · O. Riba
Interface Analysis Centre, University of Bristol, Bristol, UK
e-mail: Dr.M.Dickinson@googlemail.com

R. J. Barnes
Department of Engineering Science, University of Oxford, Oxford, UK

G. M. Hughes
Department of Materials, University of Oxford, Oxford, UK

Introduction

Metallic nanoparticles, defined by a diameter between 1 and 100 nm and characterised by a high surface area to volume ratio and high surface energy (Lien and Zhang 1999), have been widely applied for the remediation of contaminated waters. Iron nanoparticles in particular have been the subject of much study and have been shown to be efficient and cost effective at remediating a range of contaminants, including heavy metals, radionuclides, chlorinated

organics and inorganic anions, amongst others (Alowitz and Scherer 2002; Cao et al. 2005; Cheng et al. 2007; Choe et al. 2000; Dickinson and Scott in review a; Elliott and Zhang 2001; Joo et al. 2005; Kanel et al. 2005; Li and Zhang 2007; Lien and Zhang 1999, 2001; Liu et al. 2005; Miehr et al. 2004; Mondal et al. 2004; Nurmi et al. 2005; Ponder et al. 2000, 2001; Riba et al. 2008; Scott 2005; Shimotori et al. 2004; Wang and Zhang 1997; Xu et al. 2005; Lien and Zhang 1999; Zhang 2003).

Iron-driven remediation works via the corrosion mechanism, whereby the oxidation of the Fe is coupled with the reduction of the contaminant. The metallic iron core of the nanoparticle structure acts as the electron donor, whilst the more oxidised species sorbed on the surface act as the electron acceptors (Riba et al. 2008). The reaction may occur irreversibly, as in the case of chlorinated aliphatic hydrocarbons (CAHs) which are reduced to relatively innocuous ethane species, or reversibly as in the case of heavy metals and radionuclides (Miehr et al. 2004), where decontamination occurs via sorption and/or reduction of the contaminant onto the surface of the nanoparticles.

A more recent advancement has been the application of bimetallic iron-based nanoparticles, such as Fe/Pd (Elliott and Zhang 2001; Grittini et al. 1995; Lien and Zhang 2005, 2007; Wang and Zhang 1997; Zhang et al. 1998), Fe/Pt (Zhang et al. 1998), Fe/Ag (Xu and Zhang 2000) and Fe/Ni (Lien and Zhang 1999; Schrick et al. 2002; Zhang et al. 1998; Barnes et al. in review), whereby iron is combined/alloyed with a less active (noble) metal and consequently undergoes more rapid oxidation. The iron:noble metal couple essentially creates numerous galvanic cells wherein iron serves as the anode and is preferentially oxidised, whilst the noble metal (cathode) is protected and remains unchanged. As the iron corrodes, protons from the water are reduced to adsorbed H atoms and to molecular hydrogen at the catalytic noble metal surface (Elliott and Zhang 2001; Schrick et al. 2002). In many of these studies the bimetallic nanoparticles have proven to be more effective than their monometallic counterparts for the reduction of chlorinated hydrocarbons (Elliott and Zhang 2001; Schrick et al. 2002; Wang and Zhang 1997; Lien and Zhang 1999; Zhang 2003; Zhang et al. 1998; Barnes et al. in review) and the removal of uranium from solution (Riba et al. in preparation). However, the dissolution of Ni into solution was also found to increase as the Ni proportion was raised, an undesirable side effect as Ni itself may be regarded as a contaminant (US EPA 2000).

When manufactured via aqueous synthesis (after the method of Wang and Zhang 1997) the rapid nature of the particle-forming reaction results in the formation of poorly ordered metallic cores and surface oxide layers. It is postulated that annealing the nanoparticles will induce the reordering and recrystallisation of the metallic core and the surface oxide layer, which may subsequently enhance their remediation efficiency whilst reducing the rate of Fe- and Ni-dissolution. Vacuum annealing has previously been shown to significantly alter the bulk physical characteristics and the chemical and structural properties of the surface of monometallic Fe nanoparticles (INP) (Scott et al. 2009). The most significant changes were the reordering and recrystallisation of the bulk metallic cores (leading to the bonding of some previously discrete particles and the subsequent loss of oxide from adjoining regions) and diffusion related alterations to the surface oxide structure (including the thinning and dehydration of the surface oxide and migration of impurities (B and C) toward the surfaces).

This work presents a follow-on study to describe the structural and chemical changes induced in the more complex iron nickel nanoparticles (INNP) by annealing within a vacuum. As previously, a multi-disciplinary approach was used which included X-ray diffraction (XRD) to determine the changes in bulk structure; X-ray photoelectron spectroscopy (XPS) to examine the changes in the surface chemistry; and scanning electron, transmission electron and energy selective backscattered microscopy (SEM, TEM and ESB, respectively) to study the form, size and crystallinity of the INNP and vacuum annealed iron nickel nanoparticles (VAINNP). Sequential XPS analysis was again conducted whilst annealing the INNP on a heat stage within an XPS instrument in order to determine the rate of surface change invoked by vacuum annealing.

In a concurrent study (Dickinson and Scott in review b), annealing was demonstrated to improve the remediation efficacy of the INNP for the removal of uranium from solution, whilst the Ni dissolution over a 28-day reaction period was one-fifth lower from the VAINNP than from the INNP.

Materials and methods

Chemicals

All chemicals [iron sulphate ($FeSO_4 \cdot 7H_2O$), nickel chloride ($NiCl_2 \cdot 6H_2O$), sodium hydroxide (NaOH), sodium borohydride ($NaBH_4$)] and solvents (ethanol and acetone) used in this study were of analytical grade and all solutions were prepared using Milli-Q purified water (resistivity > 18.2 MΩ cm).

Nanoparticle synthesis and preparation

The iron:nickel alloy ($FeNi_{0.22}$) nanoparticles were made following the modified method of Schrick et al. (2002). Briefly, 6.15 g of $FeSO_4 \cdot 7H_2O$ and 1.5 g of $NiCl_2 \cdot 6H_2O$ were dissolved in 50 mL of Milli-Q water (18.2 MΩ cm) and then a 4 M NaOH solution was used to adjust the pH to the range 6.2–7. The salts were reduced to metallic nanoparticles by the addition of 3.0 g of $NaBH_4$. The nanoparticle product was isolated through centrifugation and then sequentially washed with water, ethanol and acetone (20 mL of each). The nanoparticles were dried in a dessicator under low vacuum (approx. 10^{-2} mbar) for 48 h and then stored in the oxygen-free environment of a Saffron Scientific glovebox until required.

To investigate the effect of annealing on the INNP, some of the batch was prepared on stubs and then mounted on the Peltier heat stage of a Thermo Fisher Scientific Escascope, operating at $<5 \times 10^{-8}$ mbar. The INNP were subsequently vacuum annealed for 24 h at 500 °C.

Nanoparticle characterisation

To enable XPS analysis of the INNP to be performed before, during and after annealing, approximately 0.002 g of material was loosely packed into a 100 μm deep recess on the surface of a sapphire substrate which was then mounted on the Peltier heat stage of a Thermo Fisher Scientific Escascope, operating at $<5 \times 10^{-8}$ mbar. The instrument is equipped with a dual anode X-ray source (Al Kα 1486.6 eV and Mg Kα 1253.6 eV). The INNP were vacuum annealed for 24 h at 500°, during which time, XPS profiles for Fe, C, O and B were acquired approximately every hour to determine surface chemistry to 4–5 nm depth. Al Kα radiation was used at 400 W (15 kV, 23 mA) to generate high resolution scans using a 30 eV pass energy and 200 ms dwell times. Spectra were collected and analysed using Pisces software (Dayta Systems Ltd). Charge correction was applied relative to the adventitious hydrocarbon peak at 284.8 eV. Peaks were curve fitted to χ^2 values <2 after suitable background subtraction.

A Phillips Xpert Pro diffractometer with a Cu Kα radiation source ($\lambda = 1.5406$ A) was used for XRD analysis (generator voltage of 40 keV; tube current of 30 mA). XRD spectra were acquired over a 2θ range of 0–90°, with a 0.02° step size and a 12 s dwell time. Analysis was performed on both INNP and VAINNP to determine bulk changes. Samples were prepared by pipetting the appropriate amount of an acetone/INNP suspension onto a glass microscope slide and allowing the acetone to dry prior to analysis.

Morphological analysis of the nanoparticles was performed on a Zeiss NVision 40 Cross Beam system. The dual focused ion beam (FIB) and SEM capabilities of the system allows for high resolution imaging and precision milling of samples. The SEM column was operated over a range of voltages from 5 to 500 V, allowing for various levels of surface sensitivity. For images acquired at lower accelerating voltages (<1 kV), a working distance of 2–3 mm was used. High resolution images were acquired using both the inlens secondary electron and ESB detectors. The inlens detector allows high sensitivity at extremely short working distances, whereas the ESB detector, which is also situated in the SEM column, features an energy filter to isolate electrons backscattered from the sample surface of the secondary electrons emitted. The ESB highlights chemical (z) contrast. Samples were prepared by pipetting the appropriate amount of an acetone/INP suspension onto a microscope stub and allowing the acetone to dry prior to analysis.

TEM images and electron diffraction patterns were obtained with a Jeol 2010 TEM operating at 200 kV. Nanoparticle samples were mounted on copper grids (3.05-mm diameter, 200 mesh) and imaged at various magnifications to gauge average particle size and surface oxide thickness.

BET specific surface area was measured using the nitrogen adsorption method (5 point isotherm) with a Micrometrics Gemini VI Surface Area and Pore Size Analyser.

Results

Comparison of bulk structures

The surface morphology and comparative size of the INNP and VAINNP were determined using the inlens secondary electron imaging mode of the Zeiss NVision 40 Cross Beam system (Fig. 1a, b). INNP were observed to be roughly spherical with a range of diameters between 20 and 80 nm. As previously described for iron nanoparticles (INP), individual FeNi nanoparticles were aggregated into chains, attributed to the magnetic properties of the predominantly Fe cores (Zhang and Manthiram 1997). In comparison VAINNP were observed to be a smaller size than the INNP and were also observed to be aligned in aggregated chains, Fig. 1c, d. However, particles appeared to be angular in form and many appeared faceted rather than spherical, attributed to recrystallisation during the thermal treatment (Fig. 2).

Using the ESB detector in the NVision system the density contrast between the metallic core and oxide shell in the INNP were readily identified (Fig. 1c). However, the boundaries between adjoining individual VAINNP were not so easily determined and implied the possible bonding of some particles at previously aligned 'end to end' by magnetic attractions as previously described for the vacuum annealed Fe nanoparticles (VAINP).

TEM images of the INNP (Fig. 1e) showed that the cores of individual particles were metallic surrounded by an apparently amorphous layer ascribed to surface oxide coverage. The cores were roughly spherical and in the range 10–30 nm diameter, whilst the amorphous oxide layer was 3–4 nm thick. Similar to the INP described in a previous study (Scott et al. 2009), dark mottles were visible within the metallic cores which indicated that individual particles were either polycrystalline or were comprised of isolated metal crystals (<1 nm) in an otherwise amorphous matrix.

TEM images of the VAINNP (Fig. 1f) clearly indicated the presence of particles bonded together at points of contact. Metal grains within the particle cores (highlighted by differential contrasting) were visibly larger than those observed in the INNP and in some cases were clearly observed to bridge the boundary between previously discrete particles. Resultantly, the surface oxide layer ($\sim$6-nm thick) around these particles was discontinuous at the point of bonding. In some TEM images the surface oxide film appeared to consist of two distinct regions of differing density (see Fig. 2b) with the region closest to the metallic core appearing less dense than the outermost oxide. This is tentatively attributed to the formation of boron oxide at the metal:oxide interface. Previous work (Scott et al. 2009) has also been demonstrated that boron trapped in the metallic iron structure during nanoparticle synthesis was migrated to grain surfaces during vacuum annealing and agrees well with the current results.

Bulk XRD analysis of the INNP recorded a broad diffraction peak at 43.53° 2θ and a less intense reflection at 50.74° 2θ, representative of (110) and (200) $Fe_{0.64}Ni_{0.36}$ phases, respectively (XPowder SET file 4714050), Fig. 3a. The low signal intensity and broad peak shape imply the presence of weakly crystalline, largely amorphous metallic material. Following annealing, the recorded 2θ diffraction peaks at 43.53° had shifted to a slightly higher 2θ value of 44.61° and was greatly improved in terms of both intensity and peak width, indicating a greater proportion of crystalline FeNi. The corresponding FeNi (200) and (211) reflections were also detected at 65.00° and 82.25° 2θ, respectively. The shift in the FeNi peak positions was consistent with the recrystallisation of the INNP to a more Fe-rich alloy.

Using XPowder software (www.XPowder.com) to create a Williamson–Hall plot (see Flewitt and Wild 2003) it was possible to calculate the average size of the metal crystallites from the measured peak breadths of the recorded FeNi (110) and (200) peaks as 1.25 nm in the INNP and 6.52 nm in the VAINNP. Curve fitting analysis, using Pisces (Dayta Systems Ltd), of the predominant FeNi peak at 43.6° and 44.61° 2θ in the spectra acquired from INNP and VAINNP, respectively, was performed to determine the relative contribution of amorphous and crystalline FeNi alloy, Fig. 3b, c. Results indicated a 74% contribution from amorphous FeNi to the FeNi(110) peak of INNP, but only a 28% contribution in the signal from XRD analysis of VAINNP. From this result, we can tentatively indicate the proportion of metallic alloy in the nanoparticles was increased 1.5 times as a result of vacuum annealing. This is in good agreement with TEM observations.

As previously described for the INP, iron boride phases were also detected following annealing, characterised by reflections at 43.25°, 47.29°, 48.34°,

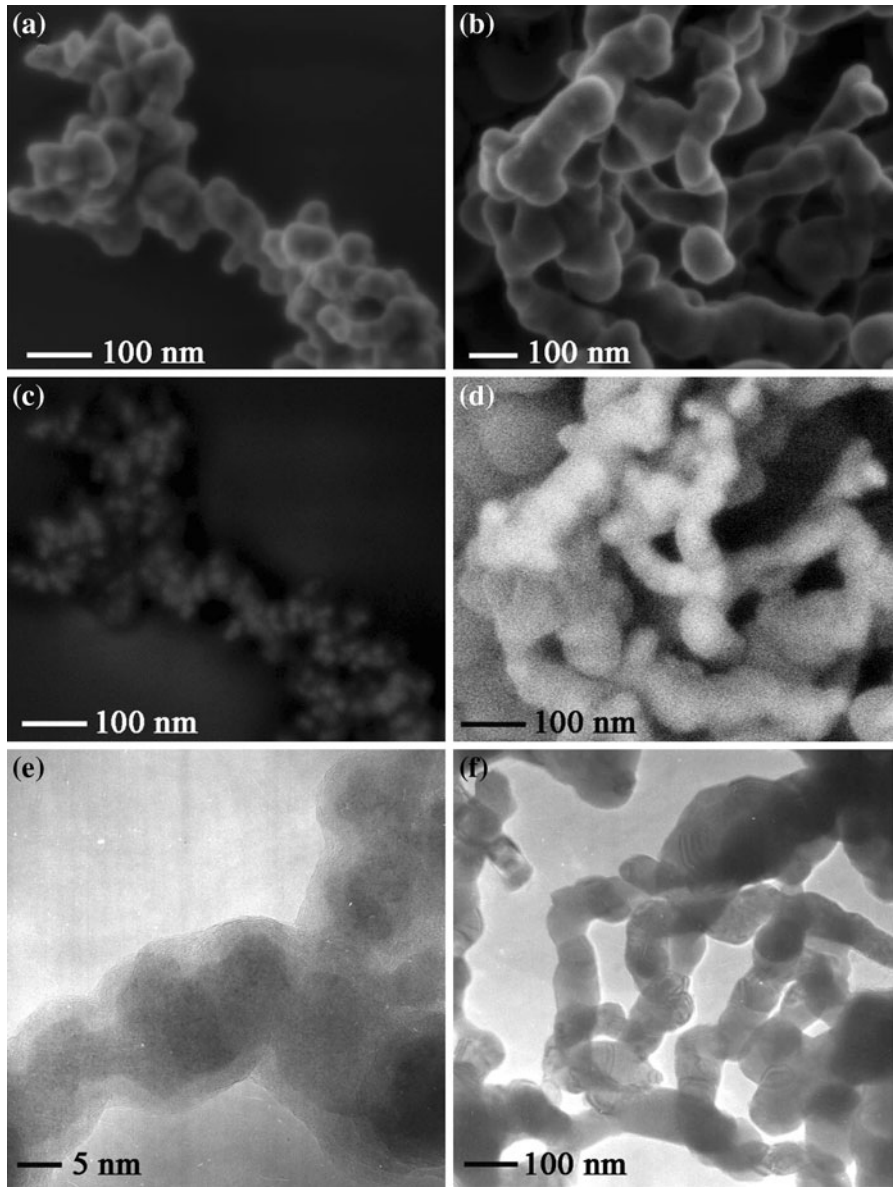

Fig. 1 Electron microscopy of the INNP and VAINNP; **a** secondary electron image of INNP, **b** secondary electron image of VAINNP, **c** energy selective backscatter image of the INNP, **d** energy selective backscatter image of the VAINNP, **e** transmission electron image of the INNP and **f** transmission electron image of the VAINNP

56.71° and 79.97° 2θ. The peak positions are consistent with Fe_xB phases, where $2 < x > 3.5$ (after Krämer et al. 1994; Dehlinger et al. 2003; XPowder ref. file 429157). The presence of this Fe_xB phase is ascribed to the crystallisation of the small amount of B originally incorporated into the INNP as an impurity during aqueous synthesis, within the FeNi lattice.

Comparison of surface chemistry

BET analysis indicated that the surface of the INNP was markedly greater than the VAINNP, recording values of 44.88 and 8.08 $m^2\ g^{-1}$, respectively. This is in good agreement with the TEM observations which indicate the bonding of individual particles at points of contact, thereby decreasing the total surface area.

Differences in the surface chemistry of the INNP and VAINNP were determined using XPS analysis that provided chemical characterisation to a depth of 4–5 nm. Of particular interest were the recorded surface proportions and chemical states of Fe, Ni, O, C and B.

As expected from the previous study of INP, changes induced in the outermost 5 nm of the

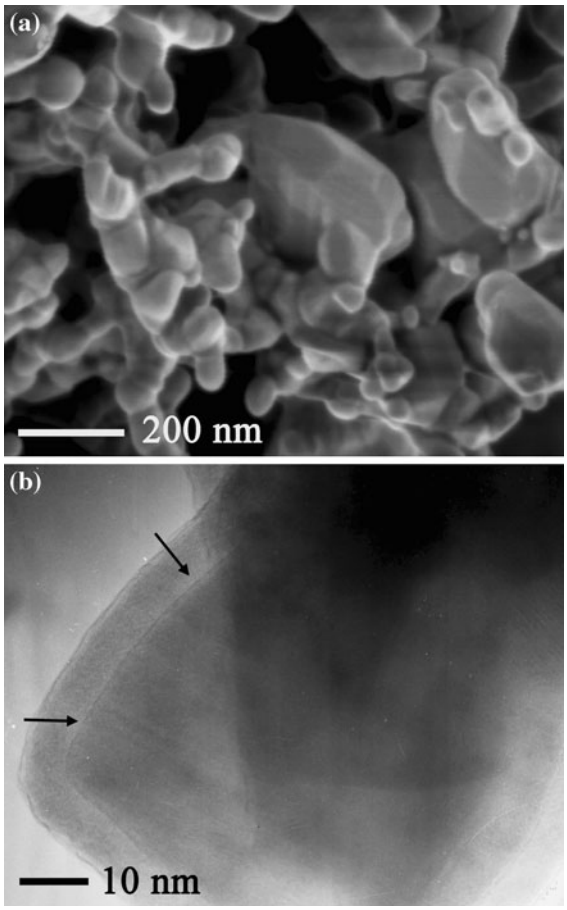

Fig. 2 Electron microscopy images of the VAINNP showing the faceted structure; **a** secondary electron image and **b** transmission electron image, differing oxide contrast is indicate with *arrows*

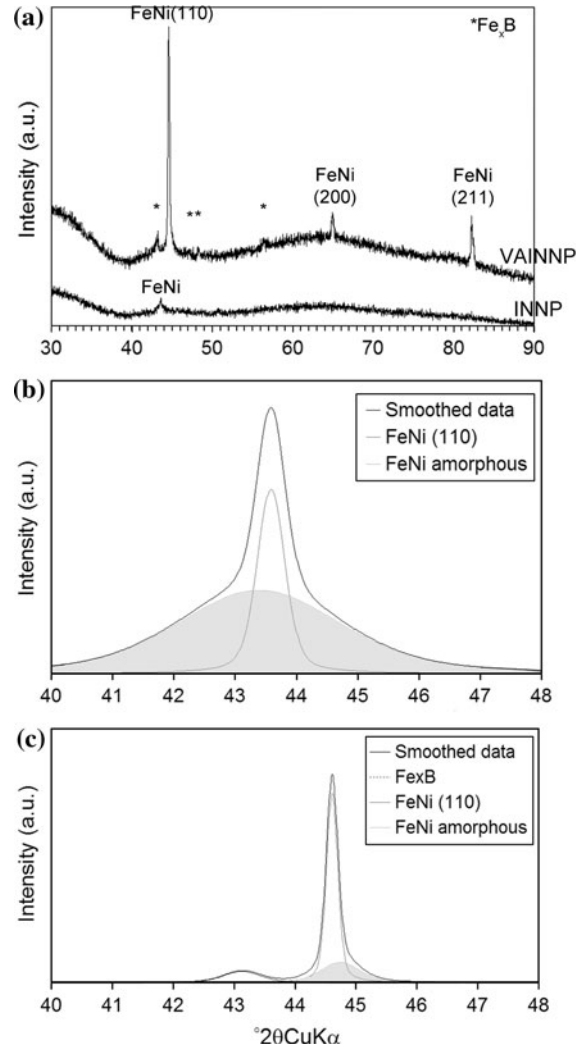

Fig. 3 XRD spectra acquired from the INNP before and after annealing; **a** spectra in the range 30–90° 2θ, **b**, **c** the curve-fitted FeNi(110) peak showing the contributions from metallic iron and amorphous iron phases, for **b** INNP and **c** VAINNP

particles by the vacuum annealing process were evident from XPS analysis of the recorded Fe2p profiles for INNP and VAINNP. The analysis volume was assumed to consist predominantly of the surface oxide with only a small contribution from the underlying metal to the recorded photoelectron signal. In order to determine the relative proportions of Fe^{2+} and Fe^{3+} in the sample analysis volume, curve fitting of the recorded Fe2p photoelectron peaks (corrected to the binding energy of the adventitious hydrocarbon) was performed using the method of Grovesnor et al. (2004). The Fe2p profile was fitted using photoelectron peaks at 706.7, 709.1, 710.6 and 713.4 eV corresponding to Fe(0), $Fe^{2+}{}_{\text{octahedral}}$, $Fe^{3+}{}_{\text{octahedral}}$, $Fe^{3+}{}_{\text{tetrahedral}}$, see Table 1. These parameters were selected on the basis that the surface oxide was assumed to be predominantly magnetite (Fe_3O_4) with some possible wustite $(FeO)_6$. In both oxides the Fe^{2+} exists in the same octahedral coordination with surrounding oxygen atoms.

Results of curve fitting indicate that after annealing the proportion of metallic iron, Fe(0), relative to Fe^{2+} and Fe^{3+} (i.e. Fe(0)/Fe^{2+} + Fe^{3+}) had increased from 0.13 to 0.87. This is clearly depicted in the sequential XPS profiles acquired between 0 and 48 h, Fig. 4a, and in curve-fitted profiles, Fig. 4b, c. It is also apparent that the ratio of Fe^{2+} to Fe^{3+} (Fe^{2+}/Fe^{3+}) changes following annealing, from an initial value of

Table 1 Peak parameters used to fit the XPS Fe2p and Ni2p profiles

	Binding energy (eV)	Crystal state	Reference	Method
Fe(0)	706.65	n/a	Allen et al. (1974)	Fe(0)
Fe(II)	709.1	Octahedral	Scott et al. (2005)	$CoFe_2O_4$ and Fe_3O_4
Fe(III)	710.55	Octahedral	Scott et al. (2005)	$CoFe_2O_4$ and Fe_3O_4
Fe(III)	713.35	Tetrahedral	Scott et al. (2005)	$CoFe_2O_4$ and Fe_3O_4
Fe(II)	708.3	Octahedral	McIntyre and Zetaruk (1977)	$NiFe_2O_4$ and Fe_3O_4
Fe(III)	710.6	Octahedral	McIntyre and Zetaruk (1977)	$NiFe_2O_4$ and Fe_3O_4
Fe(II)	709.5	Octahedral	McIntyre and Zetaruk (1977)	FeO
Ni(0)	852.8		Powell et al. (1981)	Ni(0)
Ni(II)	854.2		McIntyre et al. (1990)	NiO
Ni(II)	855.5		Ertl et al. (1980)	NiO

0.45, a near-stoichiometric magnetite ($\sim$0.33), to 1.05 which could represent either a sub-stoichiometric magnetite or a mixture of magnetite and wustite. The Fe2p photoelectron peaks were observed to shift to higher binding energies as a result of annealing. Most specifically, the peak ascribed to metallic Fe moved from 706.65 to 707.13 eV attributed to the transformation of the poorly crystalline FeNi to a more Fe-rich crystalline alloy (Nefedov et al. 1973).

Before annealing, the $Ni2p_{3/2}$ profile consisted of a multiplet of two photoelectron peaks that correlated well with metallic Ni and NiO, referenced as 852.8 and 854–856 eV, respectively, see Table 1. After 1 h of annealing, the Ni_{metal} and NiO peaks shifted to higher binding energies and the relative intensity of the NiO photoelectron peak decreased significantly (Fig. 5c). The binding energy of the recorded NiO photoelectron peak shifted to 855.5 eV, but it was not possible to further resolve the NiO peak into specific oxide phases. Quantification of the XPS data showed the initial proportion of metallic nickel, Ni(0), relative to Ni oxide in the INNP to be 0.37. Similar to the observed disproportionation of the Fe oxide, after annealing the ratio of metallic nickel had increased to 0.80. The quantitative data shown in Fig. 5c shows that the NiO disassociated more rapidly than was observed for its Fe-oxide counterpart (Fig. 6, Table 2).

An additional change in the surface composition as a result of vacuum annealing was a recorded increase in the surface abundance of B, from 24.05 to 53.07%, Fig. 5. The most significant change occurred during the first 4 h of vacuum annealing at 500 °C. Following this initial period of rapid change, the relative abundances of Fe(0) and B in the surface volume of the particles were observed to increase at a much slower rate. The amount of C and O detected in the analysis volume was observed to decrease rapidly

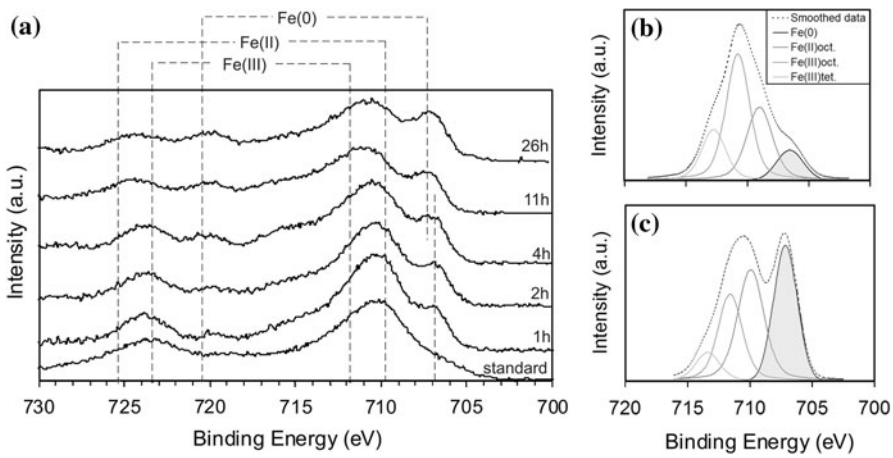

Fig. 4 XPS data acquired from INNP before, during and after annealing; **a** sequential XPS Fe2p profiles acquired at different stages of the annealing process, **b** fitted $Fe2p_{3/2}$ profile from the INNP and **c** fitted $Fe2p_{3/2}$ profile from the VAINNP. Fe(0) peaks are *shaded* for clarity

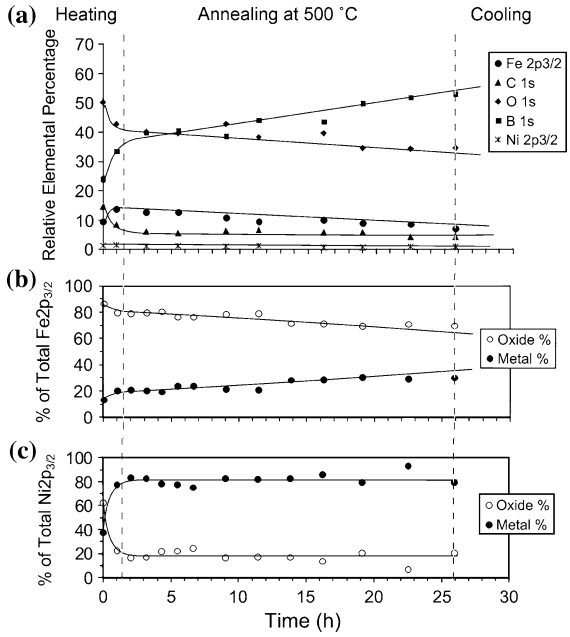

Fig. 5 The relative quantification of the surface components of the INNP during annealing; **a** the relative percentage of Fe, C, O, B and Ni, **b** the relative percentage of metal and oxide comprising the total $Fe2p_{3/2}$ photoelectron peak, **c** the relative percentage of metallic Ni and Ni oxide comprising the total $Fe2p_{3/2}$ photoelectron peak

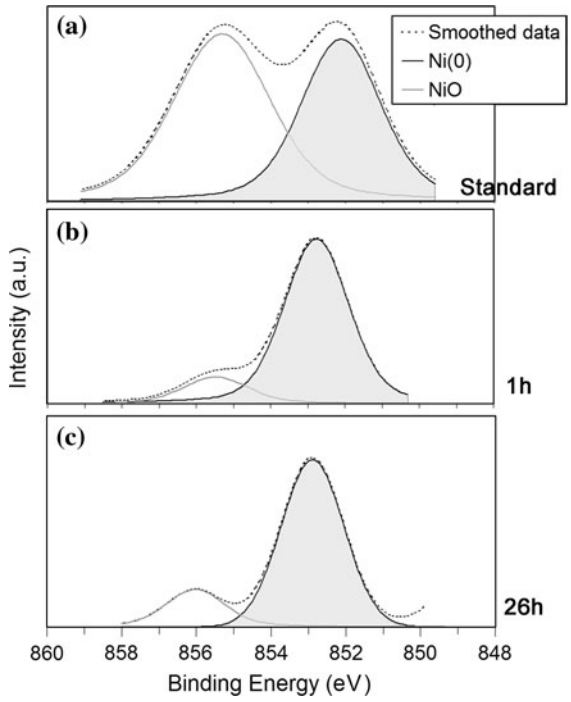

Fig. 6 Fitted XPS $Ni2p_{3/2}$ photoelectron profiles acquired from INNP before, during and after annealing; **a** INNP standard, **b** 1 h and **c** 26 h, after cooling. Ni(0) peaks are *shaded* for clarity

during the initial 4 h of annealing and then continued to decrease proportionally for the rest of the annealing period.

From an examination of the O1s spectra from the INNP prior to annealing, the amount of chemi- and physi-sorbed water on the particle surfaces was observed to be insignificant; unlike the INP described in a previous study (Scott et al. 2009). After 1 h of vacuum annealing, the recorded O1s peaks (ascribed to O in the surface oxide) were observed to shift from 530.7 eV to higher binding energies of 531.8 eV. After cooling, the recorded O1s profile was asymmetric to the low binding energy side with a primary peak recorded at 533.1 eV, attributed to the oxygen in boron oxide (B_2O_3) and a shoulder peak at 531.5 eV, attributed to the oxygen in magnetite. The B1s photoelectron peak of the INNP was centred at a binding energy of 192.1 eV indicating the presence of some B_2O_3 at the particle surfaces from the outset. Following annealing and cooling, the peak shifted to a higher binding energy (193.2 eV), consistent with the recrystallisation of the B_2O_3 phases (Joyner and Hercules 1980).

Discussion

In order to compare the physical and chemical properties of the INNP before and after vacuum annealing at 500 °C, it is necessary to consider the effects of the heating process in the absence of any significant oxygen. When the INNP are supplied with energy in the form of heat it is diffusion-related processes that allow the reorganisation of the metallic cores toward an equilibrium state, but without the incorporation of additional oxygen into the structure.

Due to the incorporation of impurities, principally boron, the initial material has a strained and poorly crystalline structure. The heat supplied during annealing drives recrystallisation and grain growth via short-range diffusion. TEM and XRD data provides clear indication that the current annealing process resulted in recrystallisation of metal grains within the INNP cores to produce what are presumably strain free equi-axed grains characterised by low-dislocation density.

Table 2 A summary of the experimental results regarding the bulk and surface characteristics of the INNP and VAINNP

Parameter	INNP	VAINNP
Particle size distribution		
0–63 nm	89.96%	–
63–100 nm	7.14%	–
>100 nm	2.9%	–
Crystallinity	Highly disordered/ amorphous FeNi	Crystalline (FeNi, Fe_xB)
Crystallite dimensions	1.25 nm	6.52 nm
Oxide thickness	3–4 nm	5–6 nm
BET surface area (m^2/g)	44.88	8.08
Surface composition		
Fe	9.64%	7.19%
O	50.13%	34.57%
C	14.74%	4.13%
B	24.05%	53.07%
Ni	1.44%	1.03%
Surface chemistry		
$(Fe(0)/Fe^{2+} + Fe^{3+})$	0.13	0.87
Fe^{2+}/Fe^{3+}	0.89	1.33
$(Ni(0)/Ni^{2+} + Ni^{3+})$	0.37	0.80

An important factor to consider in INNP is that a significant proportion of the volume of a nanoparticle consists of grain boundaries, which can be as much as 30% by volume (Flewitt, private communication). The new grains form as very small nuclei and grow to completely consume the parent material, via short-range diffusion. In the precursor material each metallic particle was observed to be polycrystalline. During annealing the growth of some grains at the expense of others resulted in a coarsening of the polycrystals and, in some cases, the euhedral faceted form of some of the larger particles, which were clearly single crystals ($\leq$150 nm). Grain growth is apparent in TEM images and occurs in order to minimise interfacial energy by reducing boundary area. Grains are assumed to grow via short-range diffusion and in the case of particles adjoining each other due to magnetic attraction this diffusion process allowed metallic bonding between particles. In order for this bonding to happen, diffusion of Fe, Ni and O must occur to displace the surface oxide at these points of contact.

In the current INNP system, the primary impurity species is B which becomes incorporated into the metallic structure during the manufacturing process. XPS data indicates that both B and C (minor impurity species) are moved to the particle surfaces during annealing; this phenomenon is assumed to occur via diffusion to grain boundary surfaces. The formation of distinct separate phases as a result of annealing is evidenced in the XRD data, which shows formation of Fe_2B phases, and the XPS data, which clearly shows the presence of B_2O_3 at the particle surfaces. The migration of B to grain boundaries is consistent with previous studies on FeNi alloys which showed the significant accumulation of B at grain boundaries as a result of diffusion induced by thermal cycling (Caceres et al. 1989a, b; Younes et al. 1992).

Another significant effect of the vacuum heat treatment on the oxide surface of the particle is similar to the metal diffusion processes on the bulk, it will result in diffusion-related alteration of the oxide structure. In comparison to vacuum annealing of the pure iron nanoparticles, the INNP displayed greater volumes of oxide disproportionation. This is clearly evidenced in the XPS results which show a decrease of the surface iron oxide thickness and a change in its stoichiometry; an increased proportion of Fe(0) and Ni(0) to Fe- and Ni-oxides, respectively, as well as a change in the Fe^{2+}:Fe^{3+} ratio. Given the melting point of wustite (FeO), magnetite (Fe_3O_4) and trevorite ($NiFe_2O_4$) are 1,377 °C, 1,583–1,597 °C

(Cornell and Schwertmann 2003) and ~1,700 °C (Kenkmann et al. 2005), respectively, the loss of surface iron oxide is attributed to the diffusion of oxygen into the metallic cores and the redistribution of oxygen to form B-oxide at the expense of Fe- and Ni-oxides. By comparing the XPS-determined ratios of metallic iron and nickel to oxide as annealing progressed it was evident that diffusion occurred most rapidly in the initial stages of annealing (0–4 h).

Figure 7 illustrates the perceived structural transformation of an idealised INNP before and after the vacuum heat treatment. It is postulated that during vacuum annealing the boron oxide forms at the metal:oxide interface, beneath the pre-existing iron oxide layer. This would account for the less dense region of the oxide observed in the TEM and also accounts for the measurements of greater oxide thickness in the VAINNP.

The BET results also indicate a physical reordering and optimisation of the surface area of the INNP. In aqueous conditions the reactivity of the VAINNP is expected to be different to the INNP. Corrosion of the particle surfaces is expected to proceed more rapidly for INNP due to the greater surface area and greater density of surface defects and dislocations. Any galvanic phenomena that may assist with surface redox reactions would be expected to be enhanced in the VAINNP due to the optimised structure of the magnetite overlayer. In using elemental metals for remediation of contaminants in groundwater, a key aspect of the decontamination is that reactions are mediated by the availability of electrons supplied by the metal, either directly at the metal surface or through conductive oxide films such as magnetite Fe_3O_4 (Riba et al. 2008). Electron availability may be limited by the presence of non-conductive surface phases such as Fe_2O_3 and FeOOH which will inhibit electron transfer. The results clearly indicate an initial and increasing abundance of B-oxide at the particle surfaces as a result of annealing. B accounted for up to 50% of the surface signal for VAINNP and the presence of a surface B-oxide layer is considered to provide a passivating layer that may inhibit corrosive degradation in aqueous environments relative to INNP. It is not clear whether the layer of B-oxide would also limit remediation reactions with contaminant species by blocking electron transfer from the metallic particle cores.

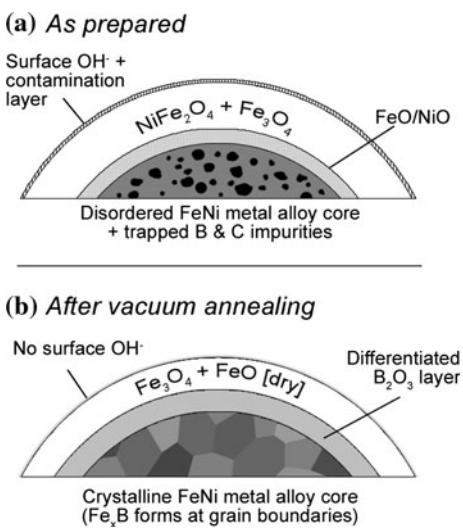

Fig. 7 An illustration of the perceived structural transformation of an idealised INNP **a** before and **b** after the vacuum heat treatment

However, reductive removal of contaminants can only proceed once contaminant species are in direct contact with the reactive surfaces. This necessitates that any of the surface reaction must be preceded by adsorption of a contaminant ion to an available surface site. The reduction in surface area induced by vacuum annealing would proportionally reduce the number of available surface adsorption sites and thus would be expected to reduce the mass of contaminants remediated on the particle surfaces. Whether there will exist a compromise between the reduced surface area and the enhanced galvanic capability on the reactivity of the VAINNP in relation to INNP remains to be determined. A concurrent study is being performed to determine the comparative efficacy of the INNP and VAINNP for the remediation of U-contaminated solutions, with a view to improving their industrial application and reactive lifetime (Dickinson and Scott in review b).

Conclusion

Vacuum annealing at 500 °C has been demonstrated to induce structural and chemical changes in INNP, which are considered to alter the subsequent reactivity with aqueous contaminants. XRD and TEM data indicates reordering and recrystallisation of the bulk metallic cores, an increase in grain size and elimination of defects and impurities, and the conversion of a significant fraction of the amorphous iron nickel alloy

to crystalline material. XPS and BET indicates significant alteration of the particle surfaces involving reduction of surface area, in addition to slight thickening and reordering of the surface oxide to incorporate a boron oxide layer following the migration of impurities to the surfaces. XPS indicated that the formation of boron oxide occurred concurrently with the partial disproportionation of iron and nickel oxides. The chemical and structural changes imbued by vacuum annealing may promote improved corrosion resistance which consequently may prove favourable for applying remediation technologies more effectively in natural and industrial situations.

Acknowledgements We thank Dr Sean Davis of the Department of Chemistry, University of Bristol for performing the TEM analysis and Professors Geoffrey Allen and Peter Flewitt for valuable discussion.

References

Allen GC, Curtis MT, Hooper AJ, Tucker MJ (1974) X-ray photoelectron-spectroscopy of iron-oxygen systems. Chem Soc Dalton 14:1525–1530. doi:10.1039/dt9740001525

Alowitz MJ, Scherer M (2002) Kinetics of nitrate, nitrite, and Cr(VI) reduction by iron metal. Environ Sci Technol 36:299–306. doi:10.1021/es011000h

Barnes RJ, Riba O, Scott TB, Gardner MN, Jackman SA, Thompson IP (in review) Optimisation of nano-scale iron/nickel particles for the reduction of high concentration chlorinated aliphatic hydrocarbon solutions

Caceres PG, Ralph B, Allen GC, Wild RK (1989a) Sensitization of inconel 600. 1. Scanning auger and optical microscopy. Philos Mag A 59:1119–1136. doi:10.1080/01418618908221166

Caceres PG, Ralph B, Allen GC, Wild RK (1989b) Sensitization of inconel 600. 2. Analytical electron microscopy. Philos Mag A 59:1137–1162. doi:10.1080/01418618908221167

Cao JS, Elliott D, Zhang WJJ (2005) Perchlorate reduction by nanoscale iron particles. Nanopart Res 7:499–506. doi:10.1007/s11051-005-4412-x

Cheng R, Wang JL, Zhang WX (2007) Comparison of reductive dechlorination of p-chlorophenol using Fe-0 and nanosized Fe-0. J Hazard Mater 144:334–339. doi:10.1016/j.jhazmat.2006.10.032

Choe S, Chang YY, Hwang KY, Khim J (2000) Kinetics of reductive denitrification by nanoscale zero-valent iron. Chemosphere 41:1307–1311. doi:10.1016/S0045-6535(99)00506-8

Cornell RM, Schwertmann U (2003) The iron oxides: structure, properties, reactions, occurrences and uses. Wiley-VCH, New York

Dayta Systems Ltd c/o Interface Analysis Centre. http://daytasystems.co.uk

Dehlinger AS, Pierson JF, Roman A, Bauer P (2003) Properties of iron boride films prepared by magnetron sputtering. Surf Coat Technol 174–175:331–337. doi:10.1016/S0257-8972(03)00399-2

Dickinson M, Scott TB (in review a) The application of zero-valent iron nanoparticles for the remediation of a uranium-contaminated waste effluent

Dickinson M, Scott TB (in review b) The effect of vacuum annealing on the remediation abilities of iron and iron: nickel nanoparticles

Elliott DW, Zhang W (2001) Field assessment of nanoscale biometallic particles for groundwater treatment. Environ Sci Technol 35:4922–4926. doi:10.1021/es0108584

Ertl G, Hierl R, Knozinger H, Thiele N, Urbach HP (1980) XPS study of copper aluminate catalysts. Appl Surf Sci 5:49–64. doi:10.1016/0378-5963(80)90117-8

Flewitt PEJ, Wild RK (2003) Physical methods for materials characterisation. Institute of Physics Publishing Ltd, Bristol

Grittini C, Malcomson M, Fernando Q, Korte N (1995) Hydrodechlorination of chlorinated ethanes by nanoscale Pd/Fe bimetallic particles. Environ Sci Technol 29:2898–2900. doi:10.1021/es00011a029

Grovesnor AP, Kobe BA, Biesinger MC, McIntyre NS (2004) Investigation of multiplet splitting of Fe 2p XPS spectra and bonding in iron compounds. Surf Interface Anal 36:1564–1574. doi:10.1002/sia.1984

Joo SH, Feitz AJ, Sedlak DL, Waite TD (2005) Quantification of the oxidizing capacity of nanoparticulate zero-valent iron. Environ Sci Technol 39:1263–1268. doi:10.1021/es048983d

Joyner DJ, Hercules DMJ (1980) Chemical bonding and electronic-structure of B_2O_3, H_3BO_3, and BN-ESCA, AUGER, SIMS, and SXS study. Chem Phys 72:1095–1108

Kanel SR, Manning B, Charlet L, Choi H (2005) Removal of arsenic(III) from groundwater by nanoscale zero-valent iron. Environ Sci Technol 39:1291–1298. doi:10.1021/es048991u

Kenkmann T, Hörz F, Deutsch A (2005) Large meteorite impacts III. Geol. Soc. Am. Spec. Paper 384, p 293

Krämer A, Leutenecker R, Aubertin F, Gonser U (1994) Amorphization of armco iron by boron implantation and subsequent crystallization by heat-treatment—a GEMS, X-ray and ultramicrohardness study. Hyperfine Interact 94:2367–2372. doi:10.1007/BF02063790

Li XQ, Zhang WX (2007) Sequestration of metal cations with zerovalent iron nanoparticles—a study with high resolution X-ray photoelectron spectroscopy (HR-XPS). J Phys Chem 111:6939–6946

Lien HL, Zhang WX (1999) Transformation of chlorinated methanes by nanoscale iron particles. J Environ Eng 125:1042–1047. doi:10.1061/(ASCE)0733-9372(1999)125:11(1042)

Lien HL, Zhang WX (2001) Nanoscale iron particles for complete reduction of chlorinated ethenes. Coll Surf A Physicochem Eng Asp 191:97–105. doi:10.1016/S0927-7757(01)00767-1

Lien HL, Zhang WX (2005) Hydrodechlorination of chlorinated ethanes by nanoscale Pd/Fe bimetallic particles. J Environ Eng 131:4–10. doi:10.1061/(ASCE)0733-9372(2005)131:1(4)

Lien HL, Zhang WX (2007) Nanoscale Pd/Fe bimetallic particles: catalytic effects of palladium on hydrodechlorination. Appl Catal B Environ 77:110–116

Liu Y, Majetich SA, Tilton RD et al (2005) TCE dechlorination rates, pathways, and efficiency of nanoscale iron particles with different properties. Environ Sci Technol 39:1338–1345. doi:10.1021/es049195r

McIntyre NS, Zetaruk DG (1977) X-ray photoelectron spectroscopic studies of iron-oxides. Anal Chem 49:1521–1529. doi:10.1021/ac50019a016

McIntyre NS, Chan TC, Chen C (1990) Characterization of oxide structures formed on nickel–chromium alloy during low-pressure oxidation at 500–600-degrees-c. Oxid Met 33:457–479. doi:10.1007/BF00666809

Miehr R, Tratnyek PG, Bandstra JZ et al (2004) Diversity of contaminant reduction reactions by zerovalent iron: role of the reductate. Environ Sci Technol 38:139–147. doi:10.1021/es034237h

Mondal K, Jegadeesan G, Lalvani SB (2004) Removal of selenate by Fe and NiFe nanosized particles. Ind Eng Chem Res 43:4922–4934. doi:10.1021/ie030715l

Nefedov VI, Gati D, Dzhurinskii BF, Serguhin NP, Salyn YV (1973) X-ray electron study of oxides of elements. Zh Neorg Khim 20:2307–2314

Nurmi JT, Tratnyek PG, Sarathy V et al (2005) Characterization and properties of metallic iron nanoparticles: spectroscopy, electrochemistry, and kinetics. Environ Sci Technol 39:1221–1230. doi:10.1021/es049190u

Ponder SM, Darab JG, Mallouk TE (2000) Remediation of Cr(VI) and Pb(II) aqueous solutions using supported, nanoscale zero-valent iron. Environ Sci Technol 34:2564–2569. doi:10.1021/es9911420

Ponder SM, Darab JG, Bucher J et al (2001) Surface chemistry and electrochemistry of supported zerovalent iron nanoparticles in the remediation of aqueous metal contaminants. Chem Mater 13:479–486. doi:10.1021/cm000288r

Powell CJ, Erickson NE, Jach T (1981) Accurate determination of the energies of auger electrons and photo-electrons from nickel, copper, and gold. J Vac Sci Technol 20:625. doi:10.1116/1.571409

Riba O, Scott TB, Ragnarsdottir KV, Allen GC (2008) Reaction mechanism of uranyl in the presence of zero-valent iron nanoparticles. Geochim Cosmochim Acta 72:4047–4057. doi:10.1016/j.gca.2008.04.041

Riba O, Scott TB, Ragnarsdottir KV, Allen GC (in preparation) Reactivity comparison of Fe and FeNi nanoparticles for remediation of uranium contaminated water

Schrick B, Blough JL, Jones AD, Mallouk TE (2002) Hydrodechlorination of trichloroethylene to hydrocarbons using bimetallic nickel–iron nanoparticles. Chem Mater 14:5140–5147. doi:10.1021/cm020737i

Scott TB (2005) Sorption of uranium onto iron bearing minerals. PhD thesis, University of Bristol

Scott TB, Dickinson M, Crane RA, Riba O, Hughes GM, Allen GC (2009) The effects of vacuum annealing on the structure and surface chemistry of iron nanoparticles. J Nanopart Res. doi:10.1007/s11051-009-9732-9

Scott TB, Allen GC, Heard PJ, Randall MG (2005) Reduction of U(VI) to U(IV) on the surface of magnetite. Geochim Cosmochim Acta 69:5639–5646. doi:10.1016/j.gca.2005.07.003

Shimotori T, Nuxoll EE, Cussler EL, Arnold WA (2004) A polymer membrane containing Fe0 as a contaminant barrier. Environ Sci Technol 38:2264–2270. doi:10.1021/es034601c

US EPA Technical Factsheet on Nickel (2000) The Water Supply (Water Quality) Regulations 2000. http://www.epa.gov/safewater/dwh/t-ioc/nickel.html. Accessed 2 October 2008

Wang CB, Zhang WX (1997) Synthesizing nanoscale iron particles for rapid and complete dechlorination of TCE and PCBs. Environ Sci Technol 31:2154–2156. doi:10.1021/es970039c. www.XPowder.com. Accessed 15 November 2008

Xu Y, Zhang W (2000) Subcolloidal Fe/Ag particles for reductive dehalogenation of chlorinated benzenes. Ind Eng Chem Res 39:2238–2244. doi:10.1021/ie9903588

Xu J, Dozier A, Bhattacharyya D (2005) Synthesis of nanoscale bimetallic particles in polyelectrolyte membrane matrix for reductive transformation of halogenated organic compounds. J Nanopart Res 7:449–467. doi:10.1007/s11051-005-4273-3

Younes CM, Allen GC, Wild RK, Ralph B (1992) An auger-electron spectroscopic study of boron segregation to the grain-boundaries in nickel-base alloy inconel-690. In: 12th Scandinavian corrosion congress and Eurocorr '92, vol II, pp 137–146

Zhang WX (2003) Nanoscale iron particles for environmental remediation: an overview. J Nanopart Res 4:323–332. doi:10.1023/A:1025520116015

Zhang L, Manthiram A (1997) Chains composed of nanosize metal particles and identifying the factors driving their formation. Appl Phys Lett 70:2469–2471. doi:10.1063/1.118859

Zhang WX, Wang CB, Lien HL (1998) Treatment of chlorinated organic contaminants with nanoscale bimetallic particles. Catal Today 40:387–395. doi:10.1016/S0920-5861(98)00067-4